Cluster observations of velocity space-restricted ion distributions near the plasma sheet

M. Wilber,[1] E. Lee,[1] G. K. Parks,[1] K. Meziane,[2] C. W. Carlson,[1] J. P. McFadden,[1] H. Rème,[3] I. Dandouras,[3] J.-A. Sauvaud,[3] J.-M. Bosqued,[3] L. Kistler,[4] E. Möbius,[4] M. McCarthy,[5] A. Korth,[6] B. Klecker,[7] M.-B. Bavassano-Cattaneo,[8] R. Lundin,[9] and E. Lucek[10]

Received 14 April 2004; revised 16 August 2004; accepted 11 November 2004; published 21 December 2004.

[1] We present Cluster ion observations obtained at 18 R_E in the magnetotail on 1 October 2001. According to a recent analysis, the quartet encountered a reconnection region and a tailward-moving neutral line. We examine in detail selected 3-D ion distributions, which through much of the hour following 0925 UT were non-gyrotropic. **B**-perpendicular slices of velocity space showed crescent-shaped regions. Occupied gyrophases were consistent over a wide range of parallel velocities, stable over time, and occurred unaccompanied by strong ion gyrofrequency waves. We interpret these observations as signatures of remote sensing near sharp particle gradients. In this view, distributions obtained simultaneously while Cluster straddled the current sheet are simply explained. Additionally, the computed first moments can have large transverse ($\mathbf{n} \times \mathbf{B}$) components ($\mathbf{n}$, a unit boundary normal), without net plasma transport. We infer separate O^+ layers above and below the current sheet. *INDEX TERMS:* 2748 Magnetospheric Physics: Magnetotail boundary layers; 2764 Magnetospheric Physics: Plasma sheet; 2788 Magnetospheric Physics: Storms and substorms; 7807 Space Plasma Physics: Charged particle motion and acceleration; 7811 Space Plasma Physics: Discontinuities. **Citation:** Wilber, M., et al. (2004), Cluster observations of velocity space-restricted ion distributions near the plasma sheet, *Geophys. Res. Lett.*, *31*, L24802, doi:10.1029/2004GL020265.

1. Introduction

[2] The particle dynamics of the plasma sheet during active periods have been studied extensively over the past 30 years. Within the plasma sheet boundary layer high speed bulk flows are common, and result from field-aligned streaming, rather than convection [*Williams*, 1981]. *Frank et al.* [1998] suggested that the high speed bulk flows observed in the central plasma sheet also result only from particle streaming, but the point has been debated [*Angelopoulos et al.*, 1999].

[3] During periods of strong activity, the current sheet (CS) can thin to ion gyroradius scales [*Mitchell et al.*, 1990], and particles can gain energy as their non-adiabatic motions allow them to traverse a cross-tail electric potential [*Speiser*, 1965]. Such strong gradients can also lead to non-gyrotropic ion distributions due to "remote sensing" effects [*Williams*, 1980; *Marcucci et al.*, 2004], which have been exploited to estimate magnetotail motions and plasma sheet orientations [*Owen et al.*, 1995]. *Nakamura et al.* [1991] presented 4.5 s AMPTE/IRM 3-D observations of non-gyrotropic magnetotail ions, which they speculated were a signature of gyrophase bunching. Numerous nightside Geotail observations have included non-gyrotropic ions, which typically have been interpreted as a mixture of particles with different sources and acceleration histories [*Mukai et al.*, 1998].

[4] Below we present observations from Cluster on 1 October 2001 obtained during a storm period (DST = −143). *Runov et al.* [2003] interpreted the field and plasma data from this crossing to indicate a tailward passage of a near-Earth neutral line past the spacecraft at ~0948 UT. Our focus is on non-gyrotropic measured ion distributions, which we argue result from a combination of remote sensing and pitch angle-dependent layering of ions within the tail. For those presented, remote sensing can account for very high speed perpendicular plasma moments, with no requirement for actual bulk plasma motions. A detailed particle tracking study using a model plasma sheet is described in the paper by *Lee et al.* [2004].

2. Instrumentation

[5] The ion data are from the Cluster Ion Spectrometry (CIS) instruments [*Rème et al.*, 2001], which each include a top-hat electrostatic analyzer (HIA), and a mass spectrometer (CODIF) that measures H^+, He^+, He^{++} and O^+. These sensors have an angular resolution of 22.5 × 22.5°, span energies of 0.005–38 keV q^{-1} and 0.01–38 keV q^{-1}, respectively, with geometry factors of 4.9×10^{-3} and 2×10^{-2} cm^2 sr. HIA returned full 3-D distributions accumulated over 3 spins (12 s), while CODIF cadences depended upon spacecraft. We used spin-averaged data from the fluxgate magnetometer (FGM) [*Balogh et al.*, 2001] to organize the ion observations.

3. Observations

[6] Figure 1 presents 35 min of summary data. The top 5 panels are C1 observations, and the bottom two show

[1]Space Sciences Laboratory, University of California, Berkeley, California, USA.
[2]University of New Brunswick, Frederickton, New Brunswick, Canada.
[3]Centre d'Etude Spatiale des Rayonnements/CNRS, Toulouse, France.
[4]University of New Hampshire, Durham, New Hampshire, USA.
[5]University of Washington, Seattle, Washington, USA.
[6]Max-Planck-Institut für Aeronomie, Katlenburg-Lindau, Germany.
[7]Max-Planck-Institut für Extraterrestrische Physik, Garching, Germany.
[8]Consiglio Nazionale delle Ricerche/IFSI, Rome, Italy.
[9]Swedish Institute of Space Physics, Kiruna, Sweden.
[10]Imperial College, London, UK.

0094-8276/04/2004GL020265$05.00

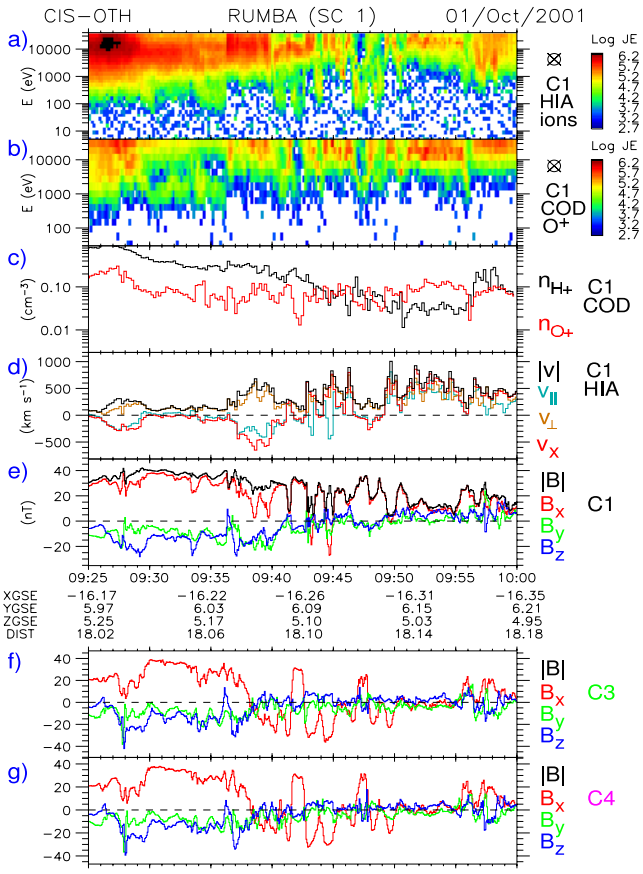

Figure 1. C1 plasma and *B* field observations, and *B* fields from C3 and C4. Energy spectrograms for (a) HIA all ions and (b) CODIF O^+; (c) CODIF densities, H^+ (black) and O^+ (red); (d) first moments from HIA projected onto *x*, $v_{\|}$ and $v_{\perp}$ directions; (e) FGM magnetic field vectors; and, below position values, FGM vectors for (f) C3 and (g) C4.

magnetic fields from C3 and C4. The HIA all-ion energy spectrogram (a) includes distributions initially from the plasma sheet, which take on a bursty character after 0943 UT. These start with a low energy threshold near 100 eV q^{-1} that increases to ~10 keV q^{-1} by 0951 UT. The CODIF O^+ spectrogram (b) shows strong fluxes, which after 0936 UT are consistently above a few keV. Figure 1c shows CODIF H^+ (black) and O^+ (red) densities. The declining trend in proton density results in O^+ dominance by ~0945 UT. Figure 1d presents components of the first moments of the HIA ion distributions, $\mathbf{v}_{1st}$, which for reasons given below we avoid calling the plasma velocity. Two high-speed tailward intervals (0926–0930 UT and 0937–0940 UT) were followed by large Earthward moments. The parallel streaming and perpendicular components were both often large contributors to the dominant *x*-component.

[7] The bottom three panels show that after starting in a high magnetic field region ($|B| \gtrsim 25$ nT), the spacecraft passed through the current sheet several times ($B_x = 0$ nT). C1 (e) twice approached, but did not quite cross, the CS between 0938 and 0940 UT, with three encounters afterwards. C3 (f) and C4 (g) did cross the CS twice during 0938–0940 UT, and several times more during 0943–0955 UT.

[8] Figure 2 presents two HIA distributions obtained by C3 during 0925–0931 UT, which are representative of the plasma sheet prior to the CS encounters. These and later distributions are presented in the spacecraft reference frame with the color scale shown. The left column shows cuts taken in the ($v_{\|}$, $v_{\perp 1}$) plane, with $\mathbf{v}_{\perp 1}$ the projection of $\mathbf{v}_{1st}$ onto a plane perpendicular to **B**. The right column shows cuts in the ($v_{\perp b}$, $v_{\perp a}$) plane taken at $v_{\|} = 0$ km s^{-1}. We wish to present **B**-perpendicular characteristics of the distributions using a consistent reference direction, and so orient these cuts along axes determined by z_{GSE} according to $\mathbf{v}_{\perp b} = \frac{\mathbf{b}\times\mathbf{z}}{|\mathbf{b}\times\mathbf{z}|}$ and $\mathbf{v}_{\perp a} = \mathbf{v}_{\perp b} \times \mathbf{b}$, with $\mathbf{b} = \mathbf{B}/B$. Thence, $\mathbf{v}_{\perp a}$ projects **z** onto the **B**-perpendicular plane, and $\mathbf{b} = \mathbf{v}_{\perp a} \times \mathbf{v}_{\perp b}$ points into the page. Components for the unit axes are provided for the two distributions. The radial red lines extending out of the boundaries on the right indicate the directions of $\mathbf{v}_{\perp 1}$ in the ($v_{\perp b}$, $v_{\perp a}$) plane.

[9] The top distribution shows convection along the $v_{\perp 1}$-axis, consistent with the tailward first moment >300 km s^{-1}. The second case shows little evidence of convection, as expected for $v_{\perp 1} < 50$ km s^{-1}. The holes in the center of each distribution reflect a lack of fluxes, not the low-energy limit (5 eV q^{-1}) of the detector. The larger hole for the second case matches the increasing low-energy cut-off seen at later times (Figure 1).

[10] During the 12-s interval 0946:12–0946:24 UT, C1 was above the current sheet while C3 and C4 were below it, and O^+ ions were dominant. Figure 3 shows an all-ion distribution from C1 and C3, and a CODIF O^+ distribution from C4. The left two columns have the same format as Figure 2. The four rightmost columns present additional **B**-perpendicular cuts at $v_{\|} = \pm 600, \pm 1200$ km s^{-1}, indicated by the colored, dotted vertical lines in the ($v_{\|}$, $v_{\perp}$) cuts (left). These reveal important 3-D information. HIA ion velocities were computed from measured energies using proton masses; the dominant O^+ ions have actual speeds 1/4 that shown. The CODIF distribution has a 1/4 smaller scale, and the perpendicular cuts were taken at $v_{\|} = 0, \pm 150, \pm 300$ km s^{-1}.

[11] Individual **B**-perpendicular cuts indicate a strong departure from gyrotropy, which is atypical of the plasma

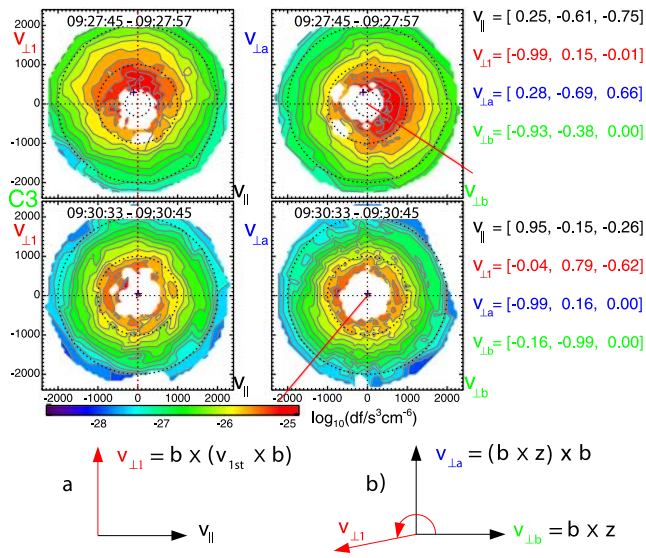

Figure 2. C3 HIA all-ion distributions from 0925–0931 UT, and schematic indicating coordinates used: (left) $v_{\perp 1}$ versus $v_{\|}$ cuts; (right) $v_{\perp a}$ versus $v_{\perp b}$ cuts at $v_{\|} = 0$ km s^{-1}.

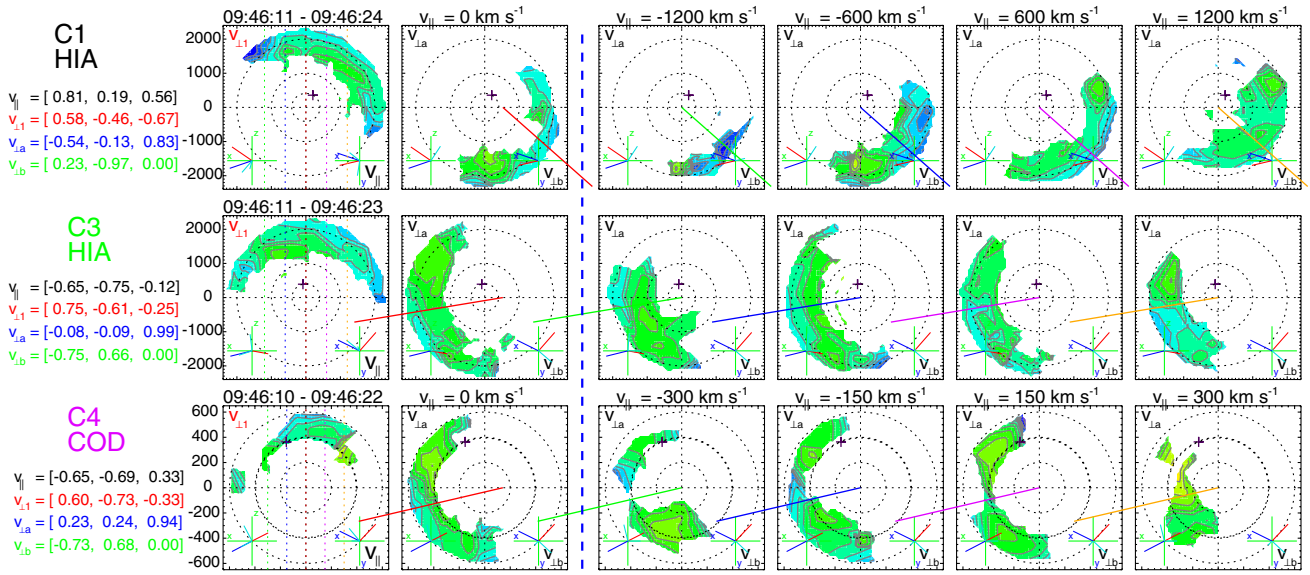

Figure 3. HIA distributions from (top) C1 and (middle) C3 when the spacecraft straddled the current sheet, and (bottom) the corresponding O^+ distribution from C4: The left column shows cuts in the ($v_{\|}$, $v_{\perp 1}$) plane, while other panels show cuts in ($v_{\perp b}$, $v_{\perp a}$) for the values of $v_{\|}$ indicated. Refer to Figure 2 for axes definitions and color scale.

sheet proper. (Gyrotropic distributions would appear circular or annular.) Across the span of $v_{\|}$, the cuts show much consistency in the velocity space regions that are occupied. C3 and C4, both south of the current sheet, show good agreement in these projections, while C1, north of the CS, appears to be reflected horizontally. Noting that B_x reverses across the CS, and that the $v_{\|}$ axis points into the page, we see that for all spacecraft the filled regions of **B**-perpendicular velocity space are roughly the same. In addition, several subsequent distributions for C3, which remained near the CS, exhibited similar form and orientations in these cuts. Near 0951:40 UT, C4 was on the same side of the current sheet as C1, and a similar situation resulted, but C3 showed reflection symmetry relative to the others.

[12] We rule out detector aliasing as an explanation for the non-gyrotropic ions. A transition between high and low density regions within a spacecraft spin could result in high fluxes being recorded in one range of azimuth angles, with low counts being collected during the remainder. However, the distributions here were integrated over three spins; aliasing effects would be reduced accordingly. Also, the 2000 km separations between the spacecraft make it unlikely that there would be any correspondence in the timing. Finally, adjacent distributions often showed similar velocity space restriction and phase.

4. Discussion

[13] We cannot account for the above distributions as non-gyrotropic populations displaced from the origin by a convective electric field; integrations that span multiple gyroperiods would tend to "wash out" structure in the **B**-perpendicular cuts. We consider three possible explanations: wave trapping, gyrophase-restricted injection, and remote sensing of shell distributions in the presence of sharp particle gradients.

[14] The wave trapping hypothesis seems implausible because the gyrophase restriction occurs over a large range of $v_{\|}$ (±2000 km s^{-1} for H^+, ±500 km s^{-1} for O^+). Resonant interaction between particles and waves occurs when the wave frequency ω matches the ion gyro-frequency Ω_i, after including the Doppler-shift ($\Omega_i = \omega \pm k v_{\|}$). For the $\Omega_i \sim$ 0.1 Hz (0.01 Hz) H^+ (O^+) gyrofrequencies typical here, the Doppler term is inconsequential over the observed range of $v_{\|}$ only for wavelengths of $\lambda = 2\pi/k \gg 2\pi v_{\|}/\Omega_i \sim 2$ (8) R_E.

[15] For many of the non-gyrotropic distributions observed on this tail crossing particles travel in both directions along the field line, suggesting that either two sources or a nearby mirror point are required if produced by gyrophase-restricted injection. Constraints can be placed upon the particle travel distances L by noting the strong coherence seen for different values of $v_{\|}$ The gyration phase for a particle travelling with a speed $v_{\|}$ will be $\phi = \phi_0 + \Omega_i L / v_{\|}$, given an initial phase ϕ_0. Assuming a common source but possibly different travel distances due to mirroring, the vanishingly small gyrophase difference found between two $v_{\|}$ cuts can be expressed as $\delta\phi = \Omega_i(L_1/v_{\|1} - L_0/v_{\|0}) \ll 1$. (Note that this diverges when $v_{\|} = 0$ km s^{-1}, indicating that all phases would be present.) For the O^+ distributions in Figure 3, the same regions of **B**-perpendicular velocity space are populated for $v_{\|}$ values of 0, ±150 and ±300 km s^{-1}. We would have to conclude that for each of the many distributions of this form found, the spacecraft were situated between a source and a very close mirror point, such that for the various parallel velocities the travel times were

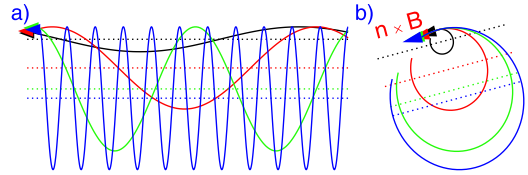

Figure 4. Trajectories of particles detected at different pitch-angles in (a) ($v_{\|}$, $v_{\perp}$) projection, and (b) ($v_{\perp b}$, $v_{\perp a}$) cuts.

negligible, and we were observing the injection phase. Similar constraints must apply at different times for spacecraft separated by up to 0.3 R_E along x_{GSE} and z_{GSE}, and 0.1 R_E along y_{GSE}.

[16] The wave trapping and gyrophase-restricted injection hypotheses are both unable to account for the uniformity of distributions observed in **B**-perpendicular cuts across the range of $v_{||}$ values (Figure 3). However, this consistency is a direct outcome for remote-sensing. Figure 4 presents schematically the trajectories of simultaneously-detected ions of equal energy with pitch angles of 10° (black), 35° (red), 60° (green) and 85° (blue). The left (right) panel shows a $v_{||}$ - $v_{\perp}$ (**B**-perpendicular) projection, under the assumption of constant field strength. We don't expect a uniform field near a thin current sheet, but the sketch correctly indicates the qualitative result where nearly field-aligned particles sample adjacent regions of space and perpendicular ions sample much larger volumes. Pitch angle-dependent differences in phase space density can therefore be associated with guiding center distance (horizontal lines in left panel), although other interpretations can be appropriate.

[17] In the right panel, nearly-horizontal dotted lines represent isocontours of density, indicating the orientation of a particle layer. (Real trajectories would include gradient drifts, and for sufficiently energetic particles could cross the CS.) If the gradient is downward in this figure, guiding centers above the spacecraft will be populated by few particles, leading to an asymmetry in fluxes for different arrival directions. For positively-charged ions (**B** is into the page), the net arrival direction is along $\mathbf{n} \times \mathbf{B}$ ($\mathbf{n}$ the boundary normal). This is independent of $v_{||}$, and also is in contrast to net fluxes along $\mathbf{n}$, typical of convective plasma motions. The gyrophase consistency seen in **B**-perpendicular cuts spanning a range of $v_{||}$ (Figure 3), the stability in the orientation of the populated phase space that can extend over several integrations, and the similar distributions seen simultaneously for spacecraft on the same and opposite sides of the CS, all can be placed within this framework of remote-sensing [*Lee et al.*, 2004]. The boundary normals inferred from inverting $\mathbf{v}_{1st} \sim \mathbf{n} \times \mathbf{B}$ indicate O^+ layers for Figure 3 that are *exterior* to the CS—a bifurcated O^+ layer.

[18] The distributions presented here all lack low-energy particles. Remote sensing places constraints on the observed values of $v_{\perp}$ but not on $v_{||}$, so this observation requires a source distribution that lacks low energy particles. The energy spectrogram in Figure 1 shows such a threshold at a few keV, and Figure 2 suggests that the plasma sheet distributions may be evolving into a shell-like form. One proposed mechanism has these particles initially accelerated through a cross tail potential, injected onto plasma sheet boundary layer field lines as beams, and then spreading in pitch angle as the result of adiabatic unfolding [*Onsager et al.*, 1991].

[19] As *Runov et al.* [2003] have noted, the first moments have strong perpendicular components. We suggest, however, that the best interpretation for these is not always one of rapid local plasma motion, but at times is due to remote sensing. In much the same way that diamagnetic currents in cold plasmas can result with very little charge transport, remote sensing in the presence of sharp density gradients can lead to non-zero first moments without bulk plasma motions. The form of distribution shown in Figure 3 is not unique, and can be seen consistently on C3 during the interval 0950–0955 UT, while this spacecraft dithered at a constant distance from the current sheet. Similar distributions have been seen on other plasma sheet crossings.

[20] **Acknowledgment.** Work at U.C.B. was supported by NASA grant NAG5-11804.

References

Angelopoulos, V., et al. (1999), Comment on "Geotail survey of ion flow in the plasma sheet: Observations between 10 and 50 R_E" by W. R. Paterson et al., *J. Geophys. Res.*, *104*, 17,521–17,525.

Balogh, A., et al. (2001), The Cluster magnetic field investigation: Overview of in–flight performance and initial results, *Ann. Geophys.*, *19*, 1207–1217.

Frank, L. A., et al. (1998), Advances in the physics of the Earth's magnetotail, in *New Perspectives on the Earth's Magnetotail*, *Geophys. Monogr. Ser.*, vol. 105, edited by A. Nishida, S. W. H. Baker, and D. N. Cowley, pp. 167–179, AGU, Washington, D. C.

Lee, E., G. K. Parks, M. Wilber, K. W. Min, and D. Y. Lee (2004), Modeling of remote sensing of thin current sheet, *Geophys. Res. Lett.*, *31*, L21806, doi:10.1029/2004GL020331.

Marcucci, M. F., et al. (2004), Energetic magnetospheric oxygen in the magnetosheath and its response to IMF orientation: Cluster observations, *J. Geophys. Res.*, *109*, A07203, doi:10.1029/2003JA010312.

Mitchell, D. G., et al. (1990), Current carriers in the near-Earth cross-tail current sheet during substorm growth phase, *Geophys. Res. Lett.*, *17*, 583–586.

Mukai, T., et al. (1998), Dynamics and kinetic properties of plasmoids and flux ropes: Geotail observations, in *New Perspectives on the Earth's Magnetotail*, *Geophys. Monogr. Ser.*, vol. 105, edited by A. Nishida, S. W. H. Baker, and D. N. Cowley, pp. 117–137, AGU, Washington, D. C.

Nakamura, M., et al. (1991), Ion distributions and flows near the neutral sheet, *J. Geophys. Res.*, *96*, 5631–5649.

Onsager, T. G., et al. (1991), Model of electron and ion distributions in the plasma sheet boundary layer, *J Geophys. Res.*, *96*, 20,999–21,011.

Owen, C. J., et al. (1995), Average motion, structure and orientation of the distant magnetotail determined from remote sensing of the edge of the plasma sheet boundary layer with $E > 35$ keV ions, *J. Geophys. Res.*, *100*, 185–204.

Rème, H., et al. (2001), First multispacecraft ion measurements in and near the Earth's magnetosphere with identical Cluster ion spectrometry (CIS) experiment, *Ann. Geophys.*, *19*, 1303–1354.

Runov, A., et al. (2003), Current sheet structure near magnetic X-line observed by Cluster, *Geophys. Res. Lett.*, *30*(11), 1579, doi:10.1029/2002GL016730.

Speiser, T. W. (1965), Particle trajectories in model current sheets: 1. Analytical solutions, *J. Geophys. Res.*, *70*, 4219–4226.

Williams, D. J. (1980), Magnetopause characteristics at 0840–1040 hours local time, *J. Geophys. Res.*, *85*, 3387–3395.

Williams, D. J. (1981), Energetic ion beams at the edge of the plasma sheet: ISEE-1 observations plus a simple explanatory model, *J. Geophys. Res.*, *86*, 5507–5518.

M.-B. Bavassano-Cattaneo, Consiglio Nazionale delle Ricerche/Istituto Fisicadello Spazio, Interplanetario, Rome, Italy.

J.-M. Bosqued, I. Dandouras, H. Rème, and J.-A. Sauvaud, Centre d'Etude Spatiale des Rayonnements/CNRS, Toulouse, France.

C. W. Carlson, E. Lee, J. P. McFadden, G. K. Parks, and M. Wilber, Space Sciences Laboratory, University of California, Berkeley, CA 94720, USA. (wilber@ssl.berkeley.edu)

L. Kistler and E. Möbius, University of New Hampshire, Durham, NH, USA.

B. Klecker, Max-Planck-Institut für extraterrestrische Physik, Garching, Germany.

A. Korth, Max-Planck-Institut für Aeronomie, Katlenburg-Lindau, Germany.

R. Lundin, Swedish Institute of Space Physics, Kiruna, Sweden.

E. Lucek, Blackett Laboratory, Imperial College, London, UK.

M. McCarthy, Department of Earth and Space Sciences, University of Washington, Seattle, WA, USA.

K. Meziane, Physics Department, University of New Brunswick, P.O. Box 4400, Fredericton, NB, E3B 5A3 Canada.